Journal of Marine Research, 48, 335–358, 1990

Simulating the time-variable coastal upwelling during CODE 2

by Dake Chen[1,2] and Dong-Ping Wang[1]

ABSTRACT

The time-variable coastal upwelling during CODE 2 is simulated using a mixing-advection coupled model. The agreement between model results and observations is generally good. During periods of strong equatorward wind stress, shelf water is cold and weakly stratified, and a front moves offshore; during periods of wind relaxation, surface temperature rises markedly, but the subsurface front usually does not go back toward the coast. At the onset of each wind event, a quick cooling of the surface layer is first caused by wind mixing followed closely by offshore advection of upwelled cold water. Due to the combined effect of mixing and advection, convergence occurs at the shoreward side and divergence occurs at the seaward side of the front. Consequently, a double-cell circulation is formed.

1. Introduction

Coastal upwelling regions are typical oceanic areas where both advection and mixing play important roles in the water mass movement and transformation. Therefore, linear, inviscid coastal models generally have little applicability for upwelling simulation although they have been successful in predicting alongshore currents and sea level changes. In recent years, models that couple the effects of density advection and diabatic mixing have been developed, and proved to be particularly useful for simulating cross-shelf circulation and heat transport. For example, de Szoeke and Richman (1981, 1984) formulated a two-layer analytical model to study the role of wind mixing in coastal upwelling. Their results clearly show an asymmetry between upwelling and downwelling due to the combined effect of surface heating and nonlinear, irreversible mixed-layer processes. They also demonstrated how a sharp upwelling front can be formed and advected offshore, leaving behind a nearly homogeneous region. Kundu (1984) constructed a numerical coastal model using a second-order turbulence closure scheme. He paid particular attention to cross-shelf circulation patterns near the upwelling front. He pointed out that the existence of the multi-cell circulation strongly

1. Marine Sciences Research Center, State University of New York, Stony Brook, New York, 11794, U.S.A.
2. Present address: University Corporation for Atmospheric Research, Boulder, Colorado, 80307, U.S.A.

depends on the parameterization of turbulence processes. In his case, there is flow reversal near the front, but there are no closed double-cells.

The field observation of coastal upwelling has improved dramatically in recent years. For example, the densely-spaced moored array during CODE 2 has provided high-quality data sets of currents, water temperature and meteorological variables on the northern California shelf for the whole upwelling season in 1982. From these data sets the fluctuating character of shelf water response to atmospheric forcing can be clearly seen. In response to strong southward wind stress and its relaxation, water temperature drops and rises regularly with the largest signal near the surface and close to the shore. The processes involved in this upwelling-relaxation sequence have been investigated through data analysis. For example, Lentz (1987a) calculated a shelf-wide volume heat budget during CODE 2. He found that the primary balance in the fluctuating heat budget is heating and cooling of the volume in response to on/offshore advective heat fluxes in the upper 30 m. On the other hand, Send *et al.* (1987) considered the heat budget in a surface layer of 30 m depth at a mid-shelf mooring. They claimed that the heat balance during relaxations is dominated by solar heating and alongshore advection. Rudnick and Davis (1988) analyzed the same CODE 2 data in more detail. Their conclusion is that surface cooling during upwelling periods is caused first by vertical mixing followed closely by offshore advection of cold water, while warming of the surface layer during relaxations seems to be mainly caused by vertical advection.

Upwelling study has now advanced to such a stage that field verification of upwelling models becomes inevitable. Modelers can no longer content themselves with the qualitative agreement between model output and observational data at a particular location or at a particular time. Simulating the time-variable coastal upwelling, for example, during CODE 2, is highly desirable and, of course, is a great challenge to modelers. We take this challenge using a numerical model in which advection and mixing are carefully coupled. The model is originally three-dimensional, but is reduced to two dimensions in the present study for two reasons. First, the CODE data indicate that the mass and heat balances on the northern California shelf are basically two-dimensional during active upwelling when averaged over some alongshore distance (e.g., Lentz, 1987a,b). Second, our primary interest in this study is on the two-dimensional aspects of coastal upwelling, such as interaction between vertical mixing and cross-shelf advection, frontal structures, and two-dimensional heat budget. The cross section along the CODE central line is chosen as the simulation plane.

2. Data

The location and geometry of the CODE 2 (1982) moored array are shown in Figure 1. Along the central line there were four mooring stations (C2, C3, C4 and C5) located on the 60 m, 90 m, 130 m and 400 m isobaths, respectively. At each station a current meter mooring and a meteorological buoy were deployed. The moored current

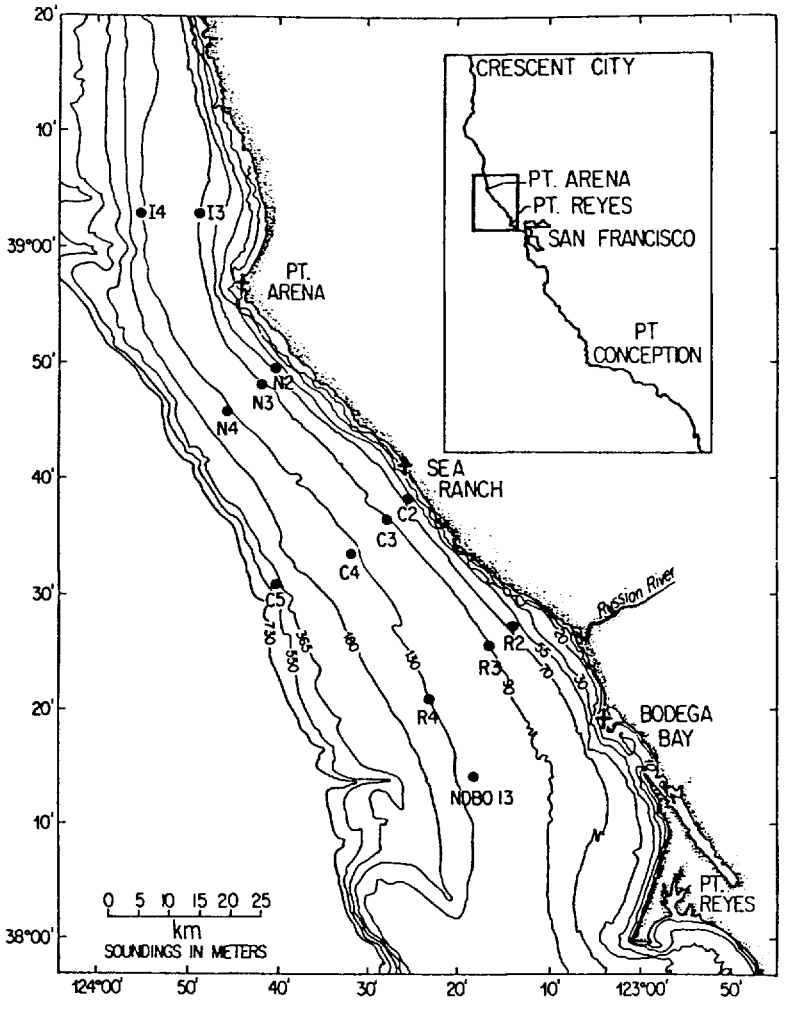

Figure 1. The CODE 2 moored array location and geometry. Solid circles represent current moorings and meteorological buoys. This figure is reproduced from Send *et al.* (1987).

meters, typically spaced 10–20 m apart in the vertical, measured water velocities as well as temperature. The sensors on the meteorological buoys measured air temperature, wind and insolation at 3.5 m above the sea surface and water temperature 1 m below the sea surface, which were used to calculate wind stress and net surface heat flux (Beardsley *et al.*, 1985; Beardsley, 1986). For a more complete description of moored current, temperature and meteorological observations, see the data reports by Winant *et al.* (1985), Irish (1985) and Beardsley *et al.* (1985). The hourly data used in the present work resulted from a block-average of the original records sampled every 4 or 7.5 min (Lentz, 1987a). Wind stress and currents were decomposed into alongshore

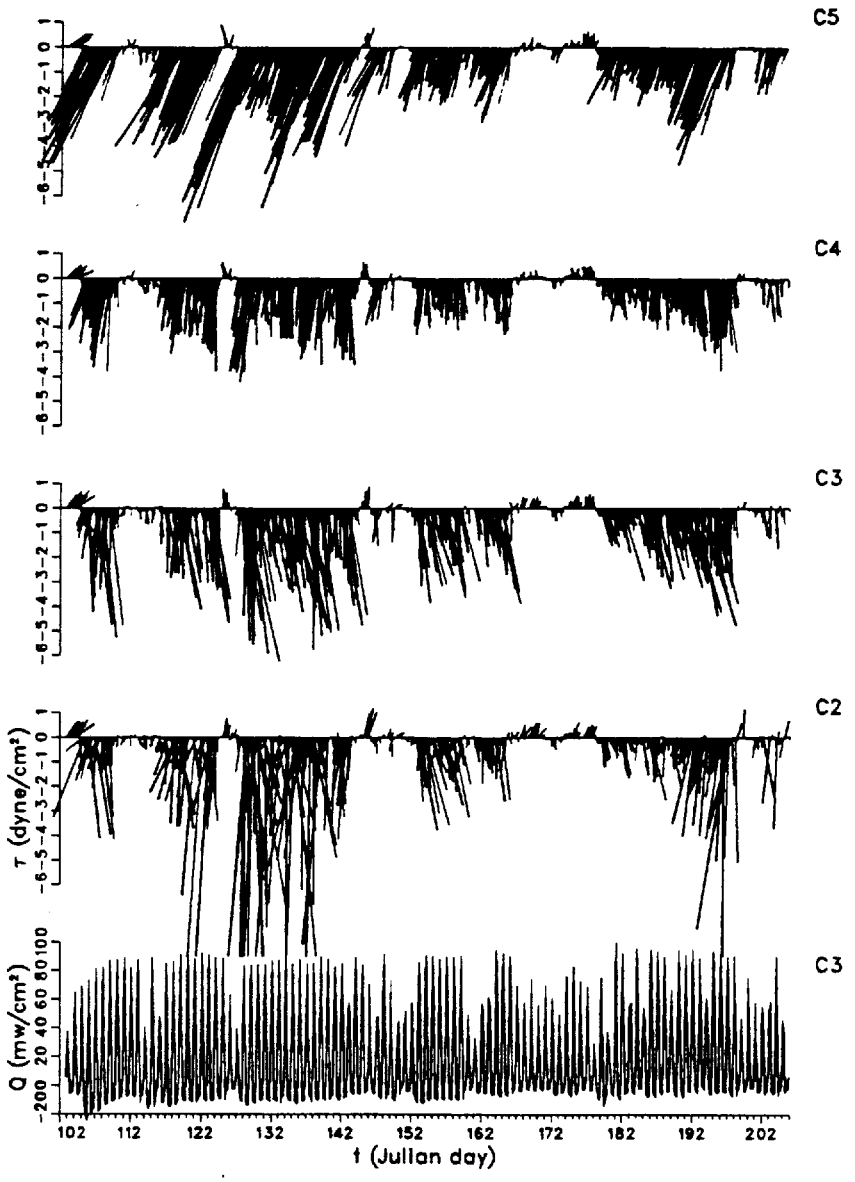

Figure 2. Time series of the wind stress vector at each mooring on the C line and the net surface heat flux at C3 mooring.

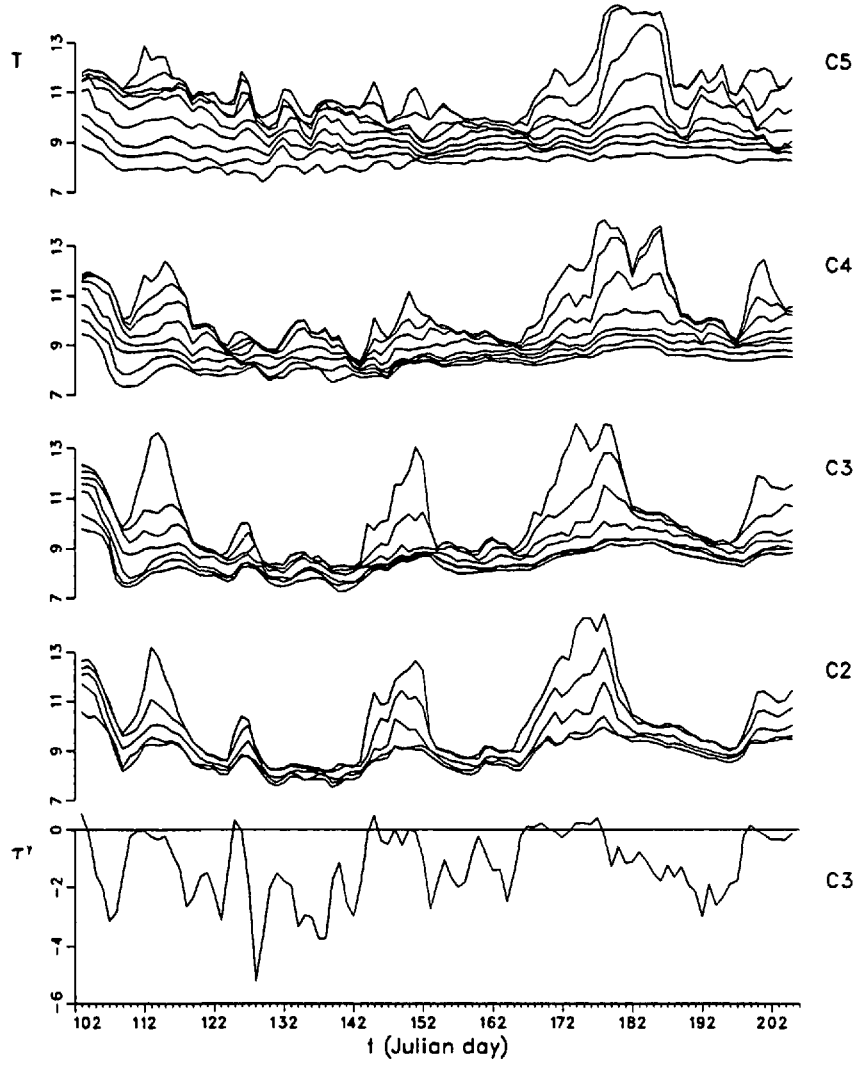

Figure 3. Time series of the observed temperature at each mooring on the C line and the wind stress at the C3 mooring. Units are °C and dyne/cm^2. At C5 the temperature observations are at 0 m, 10 m, 20 m, 35 m, 55 m, 70 m, 90 m, 110 m and 150 m, while at C2, C3 and C4 they are from the first 5, 7 and 9 depths.

(positive when directed 317°T) and cross-shelf (positive when directed 47°T) components. Figure 2 shows the time series of wind stress vectors at each mooring on the C line and the net surface heat flux at C3, which were used as model forcing. Figure 3 displays time series of the water temperature at each mooring on the CODE central line and the alongshore wind stress at a midshelf mooring.

3. Model formulation

A two-dimensional circulation model and a one-dimensional mixed-layer model were formulated separately and then were coupled together to account for the combined effect of advection and mixing.

a. Circulation model. The governing equations are:

$$\frac{\partial u}{\partial t} + u\frac{\partial u}{\partial x} + w\frac{\partial u}{\partial z} - fv = -\frac{1}{\rho}\frac{\partial p}{\partial x} + \frac{\partial}{\partial x}\left(A_H\frac{\partial u}{\partial x}\right) + \frac{\partial}{\partial z}\left(A_v\frac{\partial u}{\partial z}\right), \tag{1}$$

$$\frac{\partial v}{\partial t} + u\frac{\partial v}{\partial x} + w\frac{\partial v}{\partial z} + fu = \frac{\partial}{\partial x}\left(A_H\frac{\partial v}{\partial x}\right) + \frac{\partial}{\partial z}\left(A_v\frac{\partial v}{\partial z}\right), \tag{2}$$

$$\frac{\partial p}{\partial z} + \rho g = 0, \tag{3}$$

$$\frac{\partial u}{\partial x} + \frac{\partial w}{\partial z} = 0, \tag{4}$$

$$\frac{\partial T}{\partial t} + u\frac{\partial T}{\partial x} + w\frac{\partial T}{\partial z} = \frac{\partial}{\partial x}\left(K_H\frac{\partial T}{\partial x}\right) + \frac{\partial}{\partial z}\left(K_V\frac{\partial T}{\partial z}\right) + \frac{\partial I}{\partial z}, \tag{5}$$

$$\frac{\partial S}{\partial t} + u\frac{\partial S}{\partial x} + w\frac{\partial S}{\partial z} = \frac{\partial}{\partial x}\left(K_H\frac{\partial S}{\partial x}\right) + \frac{\partial}{\partial z}\left(K_V\frac{\partial S}{\partial z}\right), \tag{6}$$

where notations are conventional and hydrostatic assumption is used. Coordinates (x, y, z) are taken onshore, alongshore and upward with the origin at the surface-coast corner. Horizontal eddy coefficients A_H and K_H are constant (5×10^5 cm^2/s). The vertical eddy coefficients A_V and K_V will be obtained from the mixed-layer submodel. Density ρ is calculated from T and S according to Fofonoff (1962). The net incoming solar radiation $I(z)$ has the form

$$I(z) = I(0)\,(I_1\,e^{z/\lambda_1} + I_2\,e^{z/\lambda_2}), \tag{7}$$

where the subscripts 1 and 2 refer to the longwave and shortwave components of insolation, and $I(0)$ is the observed surface insolation. Following Rosenfeld (1988) we took $I_1 = 0.78$, $I_2 = 0.22$, $\lambda_1 = 1.4$ m^{-1}, and $\lambda_2 = 7.9$ m^{-1}.

The finite-difference approximations for Eqs. (1)–(6) were centered-differences for the spatial gradients, leap-frog in time-derivatives, and lagged diffusion. A space-staggered grid was used, and a mode splitting technique in time was adopted to achieve computational efficiency. Detailed description of the model can be found in Wang (1982, 1985).

b. Mixed-layer submodel. The purpose of the mixed-layer submodel is to provide vertical eddy coefficients A_V and K_V which reflect the boundary layer structure. In this study, we only considered the upper boundary layer. The equations explicitly solved in the submodel are horizontal momentum equations:

$$\frac{\partial u}{\partial t} - fv = \frac{\partial}{\partial z}\left(-\overline{w'u'} + \nu\frac{\partial u}{\partial z}\right) - Du, \tag{8a}$$

$$\frac{\partial v}{\partial t} + fu = \frac{\partial}{\partial z}\left(-\overline{w'v'} + \nu\frac{\partial v}{\partial z}\right) - Dv, \tag{8b}$$

where ν is a background viscosity, D a damping factor, and $\overline{w'u'}$, $\overline{w'v'}$ the turbulent Reynolds stress. In this study, we took $\nu = 0.2$ cm^2/s and $D = 0.1f$. Reynolds stress was parameterized according to the level 2 turbulence closure scheme of Mellor and Yamada (1974):

$$(\overline{w'u'}, \overline{w'v'}) = -lqS_M\left(\frac{\partial u}{\partial z}, \frac{\partial v}{\partial z}\right), \tag{9a}$$

$$(A_V, K_V) = (lqS_M + \nu, lqS_H + \nu), \tag{9b}$$

where l is the mixing length, q the square root of twice the turbulence kinetic energy, and S_M, S_H are functions of the gradient Richardson number

$$R_i = -\frac{g}{\rho}\frac{\partial \rho}{\partial z}\Big/\left[\left(\frac{\partial u}{\partial z}\right)^2 + \left(\frac{\partial v}{\partial z}\right)^2\right]. \tag{10}$$

When R_i exceeds a critical value (0.23), $S_M = S_H = 0$, and turbulent mixing is suppressed by the density stratification. q is calculated from a simplified turbulence energy equation, and l is determined according to the vertical distribution of q. For a more detailed description of the mixed-layer model see Chen *et al.* (1988).

The velocity field in the mixed-layer submodel is independent of the velocities in the circulation model. In other words, we assume that the vertical shears for turbulence production only comes from the Ekman and near-inertial currents generated by winds. This assumption may be reasonable since geostrophic currents generally do not play an important role in the mixed-layer dynamics (Clancy and Pollak, 1983). It is also noted that strong shears usually occur during the first few hours after the onset of storm. Hence, the prediction of the mixed layer deepening is not sensitive to the presence of coherent inertial motion. On the other hand, the turbulence production (or depression) also depends on the density stratification which is controlled by both surface heat flux and advective processes. In order to consider the nonlinear interaction between advection and mixing, it is necessary to obtain density field from the circulation model which uses complete advective and diffusive equations.

c. Model coupling. As mentioned above, mixed-layer dynamics goes into the circulation model through vertical eddy coefficients $A_V(x, z, t)$ and $K_V(x, z, t)$, while advective processes affect the boundary mixing through changes in the density field $\rho(x, z, t)$. Basically, what the mixed-layer model does to the circulation model is just providing the vertical profiles of A_V and K_V which reflect the mixed layer structure. The detailed dynamical structure in the mixed-layer model is not needed as long as the structures of A_V and K_V are resolved. In principle, our approach is not different from the embedded model of Adamec and Garwood (1985) in which an integral mixed-layer model provides the mixed-layer depth for the general circulation model. The only difference is that we used a turbulence closure scheme to compute the mixed-layer so that the profiles of eddy coefficients are obtained instead of an explicit mixed-layer depth. In practice, the circulation model first provides a density field at each time step. The mixed-layer model is solved at each horizontal point to yield eddy coefficients. These coefficients are then fed back to the circulation model to generate new velocity and density fields.

One advantage of our approach is that we can achieve computational efficiency by using different vertical resolutions in the circulation model and the mixed-layer model, since advective processes do not need a vertical resolution as fine as for boundary mixing processes.

d. Initial and boundary conditions. The model domain was a vertical plane ranging from the sea surface to the bottom and from the coast to 40 km offshore (Fig. 4). In the circulation model the horizontal resolution was constant 2 km, while the vertical grid spacing varied from 5 m near the surface to 180 m in the deep water. In the mixed-layer model the vertical resolution was doubled. The simulation covered a period of 103 days from Julian day 103 (April 13) to day 206 (July 24), 1982.

The model was started from rest. Initial values of water temperature were linearly interpolated from moored array data at 0000 GMT, April 13, 1982. Contours of initial temperature are shown in Figure 4. Initial salinity was assumed uniform in the horizontal direction, while its vertical distribution was linearly interpolated from moored data at C5.

Boundary conditions are as follows. At the sea surface $z = \zeta$,

$$A_V\left(\frac{\partial u}{\partial z}, \frac{\partial v}{\partial z}\right) = (\tau_x, \tau_y), \tag{11a}$$

$$\left(K_V \frac{\partial T}{\partial z} + I, K_V \frac{\partial S}{\partial z}\right) = (Q, 0), \tag{11b}$$

where τ_x, τ_y are the x, y components of wind stress, and Q is the net surface heat flux. Wind stress at each time step and at each x grid point inshore of C5 was linearly

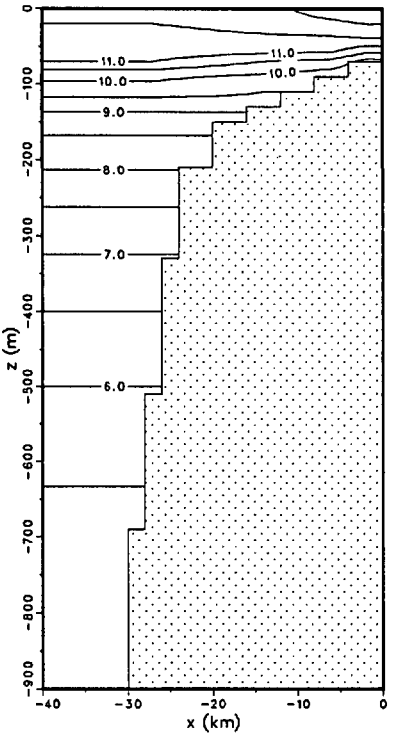

Figure 4. Model topography and initial temperature distribution. Temperature contour interval is 0.5°C.

interpolated in space and time from the hourly data at moorings C2, C3, C4 and C5. Offshore of C5 it was given the values at C5. Surface heat flux was assumed spatially uniform and was linearly interpolated in time from the hourly data at C3. At the ocean bottom $z = -H(x)$,

$$A_V\left(\frac{\partial u}{\partial z}, \frac{\partial v}{\partial z}\right) = -C_D(u^2 + v^2)^{1/2}(u, v), \tag{12a}$$

$$\left(K_V\frac{\partial T}{\partial z} + I, K_V\frac{\partial S}{\partial z}\right) = (0, 0), \tag{12b}$$

where the drag coefficient $C_D = 3 \times 10^{-3}$. At the coast $x = 0$,

$$\left(u, A_H\frac{\partial v}{\partial x}\right) = (0, 0), \tag{13a}$$

$$K_H\left(\frac{\partial T}{\partial x}, \frac{\partial S}{\partial x}\right) = (0, 0). \tag{13b}$$

At the offshore open boundary $x = -40$ km,

$$\frac{\partial \zeta}{\partial x} = 0, \tag{14a}$$

$$\frac{\partial}{\partial t}(T - T_l, S - S_l) + u\frac{\partial}{\partial x}(T, S) = (0, 0), \tag{14b}$$

where T_l, S_l are "local" parts of T, S and are calculated at the boundary using a one-dimensional version of the coupled model. Including T_l and S_l in (14b) takes account of surface fluxes and vertical mixing at the boundary. In momentum equations nonlinear terms were set to zero at the open boundary.

4. Results

Figure 5 shows the depth-time contours of model-predicted daily-mean temperature near each mooring station on the C line. Also shown is the time series of alongshore wind stress at C3. During periods of strong equatorward wind stress, shelf water is cold and only weakly stratified; during periods of wind relaxation, water temperature rises with increasing amplitude toward the surface, causing the upper layer to be re-stratified. The cooling at the onset of upwelling-favorable wind takes place rapidly and appears successively later with increasing distance from the coast, while the warming during wind relaxation is more gradual and almost simultaneous at all stations, suggesting that different processes are involved in the episodes of upwelling and relaxation.

As pointed out by Lentz (1987b), the spring transition takes two steps. At the first step (around day 107 (April 17)) the whole water column is cooled but still stratified; at the second step (around day 120 (April 30)) the stratification on the shelf is largely diminished. After the spring transition, subsurface temperatures are essentially uniform on the shelf (C2, C3 and C4). Warming episodes usually only affect a thin surface layer except around day 178 when the longest wind relaxation period is experienced. Even at this time, however, the subsurface stratification is not restored although the surface stratification is much stronger than its initial state. Thus the subsequent destratification of the water column takes place much faster than the spring transition despite more moderate wind stress. On the slope (C5), temperature changes more smoothly, and little variation is seen below 100 m after the spring transition.

Figure 6 displays cross-shelf structures of temperature, alongshore velocity, stream lines and density on day 109, 130, 178 and 197. The dots in the density plots indicate regions of density inversion ($R_i < 0$). The picture is rather classical on day 109 when the upwelling season has just started. To compensate offshore Ekman transport, upwelling occurs all over the shelf with increasing strength toward the coast. Consequently, isotherms (isopycnals) slope upward toward the coast; a front starts to appear in the surface layer; and an equatorward jet develops in accordance with the front. At

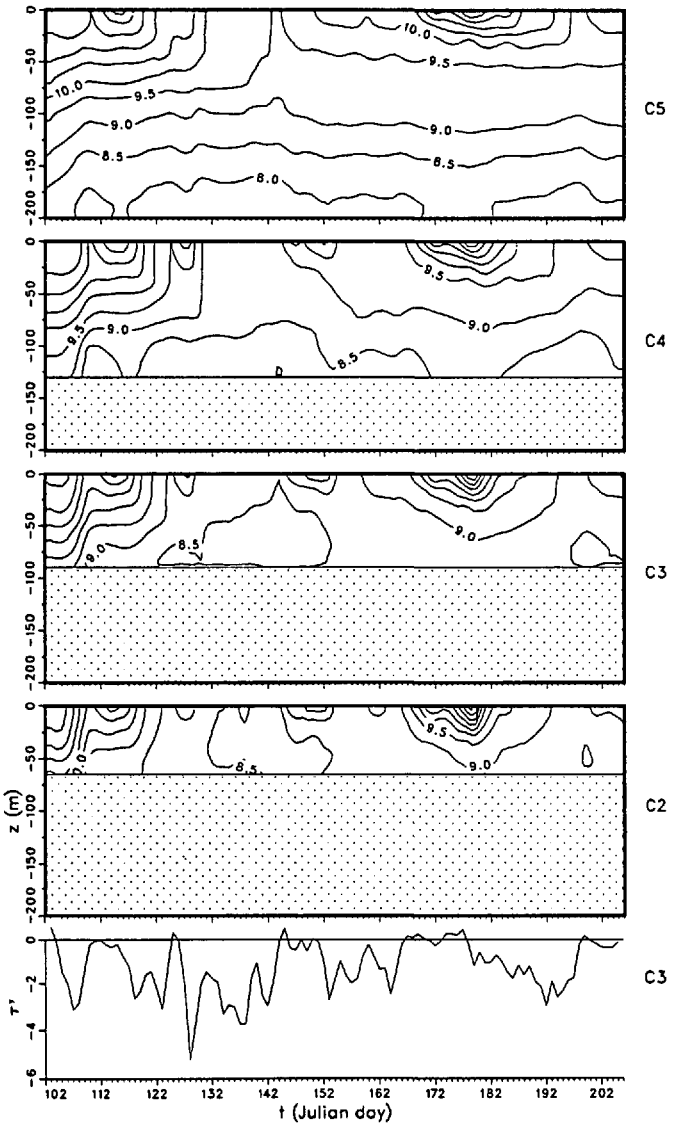

Figure 5. Model-predicted depth-time contours of temperature at each mooring station on the C line. Contour interval is 0.5°C. Also shown is the time series of alongshore wind stress at C3 (bottom). Unit of wind stress is dyne/cm^2.

this time the surface mixed layer is relatively shallow and the region of density inversion only appears in the surface layer on the seaward side of the front. It should be pointed out that the density inversion is produced in the model because the eddy diffusivity is a continuous function of Richardson number R_i. When $R_i < 0$, K_V becomes large, but not infinitely large. Therefore, the density inversion represents the

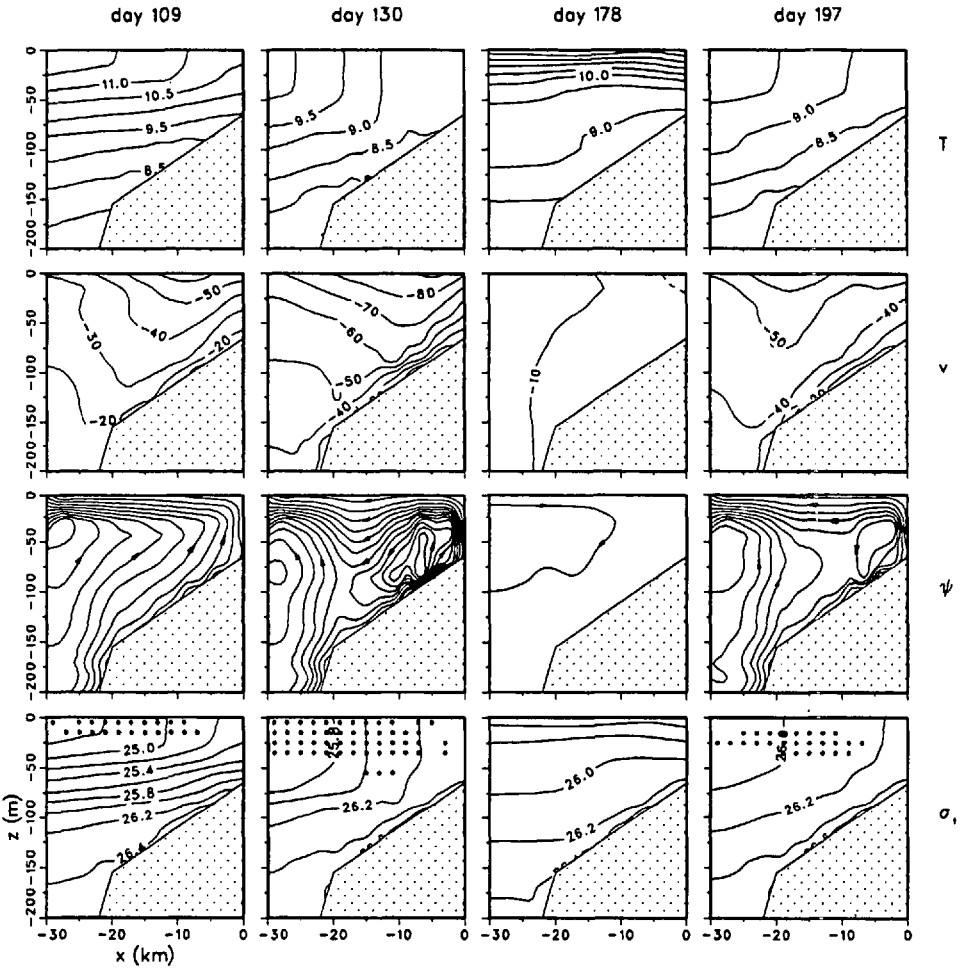

Figure 6. Model-predicted cross-shelf structures of temperature T, alongshore velocity v, stream function ψ and density anomaly σ_t on day 109, 131, 178 and 197. Dots in σ_t plots indicate the region of density inversion ($R_i < 0$). Contour interval is 0.5°C for T, 10 cm/s for v, 4000 cm^2/s for ψ and 0.2 for σ_t.

instantaneous unstable stratification and serves as an indicator of convective mixing. The picture is quite different on day 130 when the spring transition has been completed and the equatorward wind stress is the strongest. The upwelling front is strengthened and moves to the outer shelf, leaving behind a nearly homogeneous region. However, the equatorward jet shifts shoreward instead of seaward, because the cross-shelf geostrophic balance on the shelf is now modified by frictional force. The most interesting feature at this time is the cross-shelf circulation. Upwelling takes place in two narrow zones, one at the coast and the other on the seaward side of the front. On the shoreward side of the front is a downwelling zone. In association with the

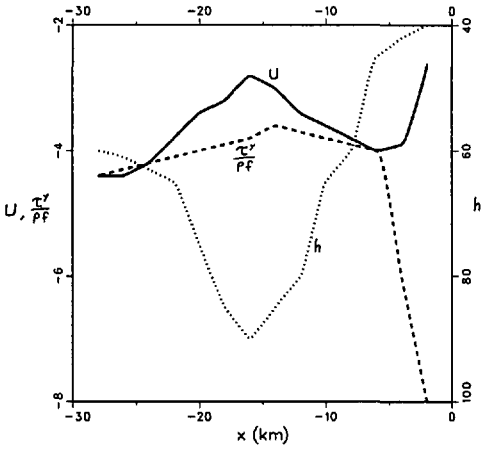

Figure 7. Cross-shelf distribution of $\tau^y/\rho f$ (dashed curve), upper layer transport U (solid curve), and the upper layer depth h (dotted curve) on day 130. Unit is 10^4 cm^2/s for $\tau^y/\rho f$ and U, and m for h.

divergence and convergence of the upper layer transport, a prominent double-cell circulation is formed.

At first glance one may think that the double-cells are caused by the cross-shelf variation of wind stress (Fig. 2). As a test, Figure 7 shows the cross-shelf distribution of daily-averaged $\tau^y/\rho f$ and the offshore transport in the upper layer on day 130. The upper layer depth, which is defined by the depth where cross-shelf velocities vanish, is also plotted in Figure 7. There is a rapid decrease of equatorward wind stress from C2 ($x = -2$ km) to C3 ($x = -6$ km), which, however, can not be responsible for the transport convergence seaward of C3. The wind variation is rather smooth seaward of C3. It accounts for at most 20% of the transport minimum around $x = -15$ km. Therefore, the cross-shelf variation of wind stress is not the primary cause of the double-cell circulation. Since an equatorward jet exists in the vicinity of the minimum offshore transport, one may also argue that the minimum transport is a result of v_x through the mechanism $U \sim \tau^y/\rho(v_x + f)$ (Niiler, 1969). In our case, v_x is at most $0.1f$ when averaged in the surface layer. Its contribution to the transport variation cannot be more than 10%.

We explain the double-cell circulation as follows. Due to the combined effect of strong wind mixing and advection, the surface mixed layer deepens rapidly, but, the deepening is not spatially uniform. At the front, the inshore upwelled cold water is advected over the offshore warm water, causing an unstable stratification and an anomalous deepening of the mixed layer, as indicated by the much deeper density inversion region there. Consequently, the surface offshore flow has a maximum depth at the front, which requires a minimum upper layer transport. If the net normal-to-shore transport is zero (as it must be in a 2-D model), the upper layer transport in a

water column of finite depth is modified in such a way that a deeper upper layer corresponds to a smaller transport (Samelson and de Szoeke, 1988). This relation can be clearly seen in Figure 7. Therefore, it is the anomalous deepening of the mixed layer at the front that causes the convergence on the shoreward side and the divergence on the seaward side of the front. The narrowness of the upwelling zones, especially the one at the coast, is a result of reduced baroclinic Rossby radius of deformation.

The picture on day 178 (Fig. 6) is typical for wind relaxation periods. Surface water is warmed everywhere and isotherms (isopycnals) are nearly level with a slight downward slope toward the coast. The alongshore current is weak, barotropic, and increasing offshore. The cross-shelf current is weak and onshore in the upper layer and offshore in the lower layer. Mixed-layer depth is very shallow and there is no density inversion at all. The picture on day 197 represents a case of moderate equatorward wind stress. Compared to day 130, the stratification on the shelf is stronger, the front is weaker and closer to the shore, and the mixed layer is shallower but still has a maximum at the front. Consequently, on day 197 a weak double-cell circulation exists with a small inner cell. The equatorward jet is in geostrophic balance with the front. One point worth noting at this time is that density inversions occur in the lower part of the mixed layer, but not in the upper part of the mixed layer where the weak offshore advection of cold water cannot overcome the surface heat flux.

Time series of the daily-mean heat budget for the upper 35 m layer at each mooring on the C line are shown in Figure 8. The thick solid curve is the rate of change of heat, the dashed curve is the advection of heat, and the thin solid curve is the vertical turbulent heat flux. For clarity, the surface heat flux, which has a nearly constant daily-mean value of 181 W/m^2, is not plotted. In this figure, cooling is implied by negative advective flux and turbulent flux. In general, the rate of change of heat in the surface layer is larger on the shelf than on the slope. At the onset of each equatorward wind event, cooling is first caused by a spurt of vertical mixing followed closely by a spurt of offshore advection, as noted by Rudnick and Davis (1988) from CODE 2 data. Time scales of these spurts are relatively long during the spring transition when shelf water is highly stratified, but are very short after the spring transition when subsurface water is uniform. For example, a strong mixing cooling occurs on day 179 at C2 for one day, followed by a strong advective cooling for 3 days, after which the cooling (destratification) of the water column is completed. Actually the time scale of mixing is even shorter. If hourly data are plotted instead of daily-mean, mixing spurts would be larger and narrower. It is interesting to note that a mixing warming occurs when the advective cooling reaches its maximum. This warming of the surface layer results from convective mixing, which partly compensates the cooling caused by offshore advection of cold water. During periods of wind relaxations, mixing and cross-shelf advection generally are not as effective as surface heating in warming of the surface layer, except during the period from day 174 to day 178 when all effects are important near the coast.

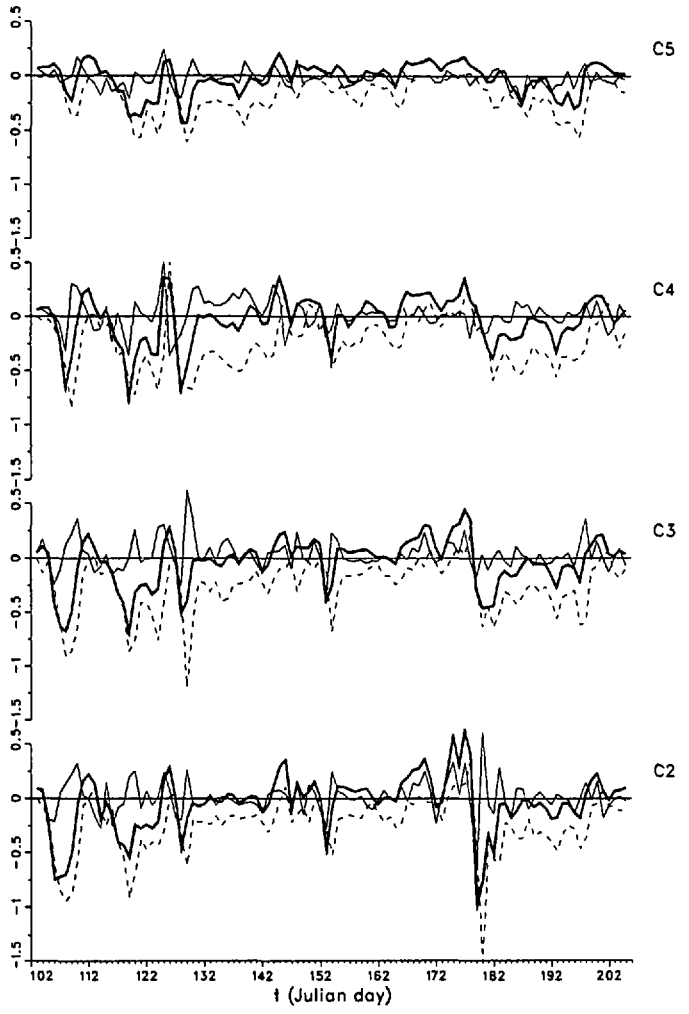

Figure 8. Model-predicted time series of heat budget in the top 35 m at each mooring on the C line. Thick solid curve is the rate of change of heat, dashed curve is the advective heat flux, and thin solid curve is the vertical turbulent heat flux. Unit is 10^3 W/m^2.

Figure 9 displays x-t contours of temperature at 2.5 m and 20 m depths. Some of the processes mentioned above are evident in this figure. At the beginning of each southward wind event, wind mixing entrains cold water into the surface layer, causing a quick drop of surface temperature. Later on, both surface and subsurface temperatures drop due to the offshore advection of upwelled cold water. During wind relaxations, surface temperature is greatly increased by the dominant surface heating; but subsurface temperature does not rise markedly except around day 175 when onshore heat advection is evident as indicated by the reversed cross-shelf currents. In general, the surface temperature is very sensitive to vertical mixing and solar heating, and it can

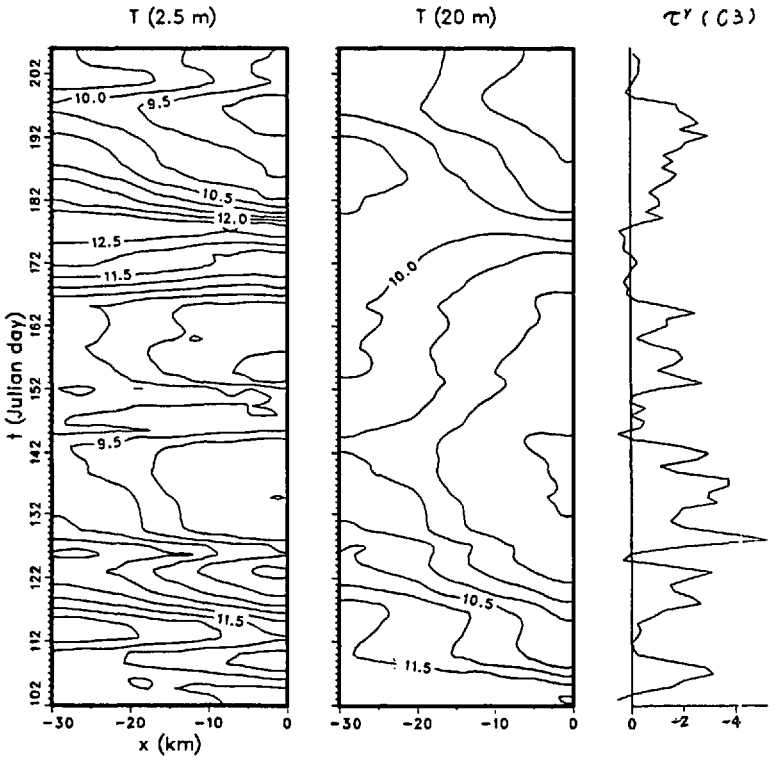

Figure 9. Model-predicted distance-time contours of temperature T at 2.5 m and 20 m depths. Contour interval is 0.5°C. Time series of the alongshore wind stress τ^y (dyne/cm^2) at C3 is also plotted.

not be reliably used as an indicator of advective processes such as frontal movement. For example, a brief wind relaxation around day 126 causes the surface isotherms to retreat toward the coast, but, this is not a real frontal movement since, as indicated by the 20 m temperature contours, the upwelling front remains stationary on the mid-shelf during the period.

5. Comparison

In this section, daily-averaged temperature and velocities predicted by the model are compared with that observed on the CODE 2 C-line. Mean values, standard deviations, and linear correlation and regression coefficients between observed and modeled variables were computed over the simulation period (103 days). Results for temperature, cross-shelf velocity, and alongshore velocity at each mooring on the C-line are shown in Tables 1, 2 and 3, respectively. At 95% confidence, correlations higher than 0.2 are significant. Regression coefficients larger (less) than 1 suggest that the model underpredicts (overpredicts) the observation. It should be pointed out that the results

Table 1. Statistics of observed and modeled temperature (°C) on the CODE 2 central line. T, σ, γ and β represent mean, standard deviation, correlation and regression coefficient, respectively. Subscript $o(m)$ denotes observed (modeled).

Mooring	Depth	T_o	T_m	σ_o	σ_m	γ	β
C2	0 m	10.3	10.0	1.6	1.4	0.91	1.1
	10 m	9.9	9.6	1.1	1.0	0.87	1.1
	20 m	9.3	9.2	0.9	0.7	0.81	1.1
	35 m	8.9	9.0	0.8	0.6	0.81	1.1
	53 m	8.4	8.9	0.6	0.5	0.70	1.0
C3	0 m	10.4	10.2	1.6	1.4	0.88	1.0
	10 m	9.8	9.7	1.0	0.9	0.94	1.1
	20 m	9.4	9.4	0.9	0.8	0.89	1.1
	35 m	9.0	9.2	0.7	0.6	0.81	1.0
	53 m	8.7	9.0	0.7	0.5	0.77	1.1
	70 m	8.6	8.9	0.6	0.5	0.72	1.3
	83 m	8.4	8.8	0.6	0.5	0.73	1.4
C4	0 m	10.6	10.8	1.4	1.4	0.80	0.9
	10 m	10.3	10.4	1.2	0.9	0.81	1.1
	20 m	9.9	10.1	0.9	0.7	0.74	1.0
	35 m	9.4	9.8	0.7	0.6	0.67	0.9
	55 m	9.0	9.4	0.6	0.4	0.63	1.0
	70 m	8.8	9.2	0.5	0.3	0.67	1.3
	90 m	8.5	8.9	0.5	0.2	0.72	1.5
	110 m	8.4	8.7	0.5	0.3	0.76	1.3
	121 m	8.3	8.5	0.5	0.3	0.72	1.2
C5	0 m	11.3	11.2	1.2	1.3	0.69	0.7
	20 m	11.1	10.5	1.1	0.7	0.45	0.9
	35 m	10.5	10.1	1.0	0.6	0.38	0.7
	55 m	10.2	9.7	0.7	0.5	0.61	1.2
	70 m	9.8	9.5	0.6	0.4	0.79	2.2
	90 m	9.4	9.1	0.4	0.2	0.78	2.5
	110 m	9.0	9.0	0.3	0.2	0.60	1.5
	150 m	8.6	8.7	0.2	0.1	0.56	1.9
	250 m	8.2	8.0	0.2	0.1	0.21	0.9
	350 m	7.6	7.4	0.2	0.1	0.03	0.1

from correlation and regression coefficients are suggestive rather than conclusive since the accurate determination of error bounds is difficult (Chapman, 1987). Direct comparison between observed and modeled mean values and standard deviations may be a better evaluation of model performance.

Observed mean temperatures are well predicted although their variances are slightly underpredicted as indicated by standard deviations and regression coefficients (Table 1). Correlations are generally high except in the deep slope water (C5). Figure 10 shows model-predicted time series of daily-mean temperature at each mooring station on the C line. Comparing it with Figure 3, we see that the agreement between model results and observations is generally good. However, the model-predicted cooling at the

Table 2. Statistics of observed and modeled cross-shelf velocity (cm/s) on the CODE 2 central line. U, σ, γ and β represent mean, standard deviation, correlation and regression coefficient, respectively. Subscript $o(m)$ denotes observed (modeled) value.

Mooring	Depth	U_o	U_m	σ_o	σ_m	γ	β
C2	10 m	−1.5	−1.8	2.8	2.6	0.72	0.8
	20 m	3.4	−0.4	4.6	1.6	0.79	2.3
	35 m	1.0	0.2	3.2	0.7	0.51	2.3
	53 m	0.0	0.7	1.0	1.0	0.14	0.2
C3	10 m	−4.7	−5.8	7.7	7.7	0.82	0.8
	20 m	−1.0	−3.4	6.4	5.7	0.74	0.9
	35 m	0.1	−1.4	4.1	3.7	0.67	0.8
	53 m	0.7	−0.5	3.0	2.0	0.58	0.9
	70 m	0.2	−0.4	1.7	1.2	0.51	0.8
	83 m	0.1	2.7	1.9	4.0	0.47	0.2
C4	10 m	−8.5	−7.6	9.9	7.8	0.75	1.0
	20 m	−4.2	−4.2	7.0	5.4	0.74	1.0
	35 m	−2.2	−1.6	6.0	3.5	0.77	1.3
	55 m	0.2	0.0	4.7	1.7	0.68	1.9
	70 m	0.5	0.5	4.3	1.3	0.61	2.2
	90 m	0.3	0.6	3.9	1.4	0.71	2.1
	110 m	−0.2	0.8	3.3	1.4	0.65	1.6
	121 m	0.1	1.9	3.2	2.4	0.41	0.6
C5	20 m	−2.6	−2.2	10.9	5.6	0.75	1.7
	35 m	0.0	−0.6	9.4	4.8	0.80	3.1
	55 m	2.3	0.1	6.8	2.5	0.73	3.4
	70 m	2.3	−0.1	5.7	1.5	0.55	2.9
	90 m	2.1	−0.2	4.6	1.0	0.59	3.0
	110 m	3.2	−0.1	5.3	0.9	0.66	3.3
	150 m	3.3	0.4	4.5	1.0	0.66	2.4
	250 m	4.0	−1.2	3.4	1.2	0.01	0.0
	350 m	2.8	−2.3	2.0	3.1	0.06	0.0

first step of the spring transition is weaker than that observed, indicating that the spring transition is not merely caused by local wind. The model also underpredicts the warming during relaxations, especially close to the shore, probably due to the omission of alongshore heat advection. Another discrepancy between model-predicted and observed temperature fields is around day 184 (July 2) when a pool of warm water was observed over the outer shelf and slope in spite of equatorward wind stress. This anomaly is a result of offshore eddy variability (Lentz, 1987a) which cannot be resolved in our two-dimensional model.

Observed mean cross-shelf velocities are well predicted in the surface layer, but not so well beneath the surface layer (Table 2). In particular, the predicted onshore flow on the shelf tends to increase to the bottom, while that does not show in the observations. This is not surprising since there is no alongshore pressure gradient in the model. Away from the boundaries, a steady cross-shelf flow cannot exist because there is no force to

Table 3. Statistics of observed and modeled longshore velocity (cm/s) on the CODE 2 central line. V, σ, γ and β represent mean, standard deviation, correlation and regression coefficient, respectively. Subscript $o(m)$ denotes observed (modeled) value.

Mooring	Depth	V_o	V_m	σ_o	σ_m	γ	β
C2	10 m	3.4	−17.6	18.4	18.6	0.77	0.8
	20 m	7.0	−12.5	18.3	14.8	0.65	0.8
	35 m	3.8	−10.4	13.1	11.0	0.51	0.6
	53 m	2.4	−9.7	8.1	9.2	0.42	0.4
C3	10 m	−4.8	−29.6	23.4	18.4	0.79	1.0
	20 m	−3.6	−24.4	23.6	16.7	0.76	1.1
	35 m	−1.4	−21.7	17.8	14.4	0.69	0.9
	53 m	0.7	−20.5	15.7	14.0	0.67	0.8
	70 m	1.3	−19.2	14.0	14.3	0.68	0.7
	83 m	1.1	−18.7	11.7	15.7	0.71	0.5
C4	10 m	−21.4	−27.7	21.3	15.8	0.74	1.0
	20 m	−16.5	−22.6	18.8	14.5	0.75	1.0
	35 m	−11.2	−19.6	15.1	12.4	0.72	0.9
	55 m	−7.4	−18.2	13.5	11.7	0.73	0.8
	70 m	−4.9	−17.3	12.4	11.7	0.75	0.8
	90 m	−2.0	−16.4	11.2	11.8	0.77	0.7
	110 m	−0.8	−15.8	9.2	11.6	0.64	0.5
	121 m	1.3	−14.7	10.4	11.2	0.74	0.7
C5	20 m	−17.0	−17.5	19.0	11.7	0.59	1.0
	35 m	−13.0	−15.1	16.0	9.5	0.52	0.9
	55 m	−8.7	−14.4	13.0	8.7	0.47	0.7
	70 m	−5.7	−14.0	11.5	9.0	0.45	0.6
	90 m	−1.8	−13.4	9.5	9.1	0.36	0.4
	110 m	0.5	−12.7	9.4	9.0	0.35	0.4
	150 m	5.5	−11.9	10.0	9.0	0.24	0.3
	250 m	11.1	−5.1	9.3	4.3	0.11	0.2
	350 m	6.4	−5.0	6.0	3.8	0.09	0.1

balance the Coriolis force associated with the flow. Standard deviations are underpredicted in the subsurface layer, especially on the outer shelf and slope. It is worth noting that the model fails to predict the mean subsurface onshore flow and the related large variance observed on the slope, indicating the dynamical process there is less controlled by the local forcing. Time series of demeaned cross-shelf velocities at 10 m depth are shown in Figure 11. In general, the model-predicted cross-shelf velocity agrees well with observation at mid- and inner-shelf moorings. However, the model fails to predict some short-scale variations in cross-shelf velocity which are not correlated with local wind. For example, a very strong offshore flow is observed at mid- and outer-shelf around day 133 when the equatorward wind is actually decreasing. This kind of feature may be related to jet-like currents.

The model is not able to predict observed mean alongshore velocities (Table 3). On the inner shelf, large equatorward mean flow is predicted while the observed means are

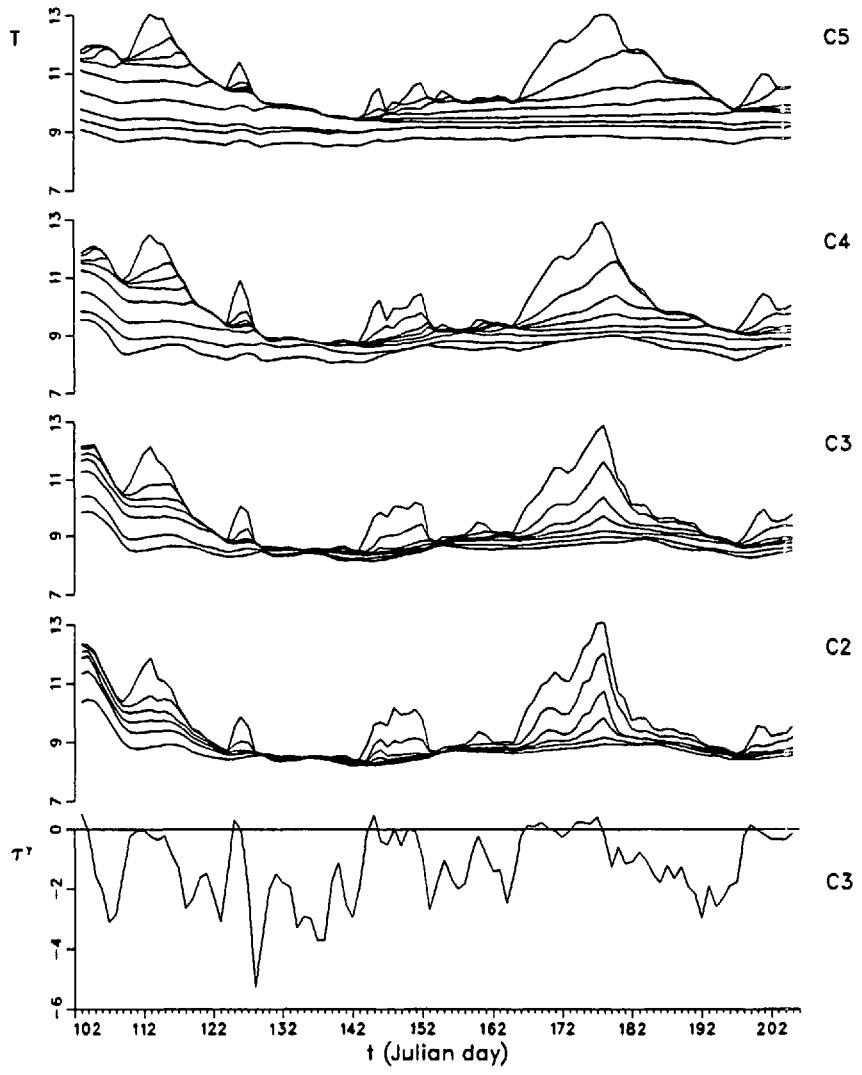

Figure 10. Time series of the model-predicted temperature at each mooring on the C line and the observed wind stress at the C3 mooring. Units are °C and dyne/cm^2. At C5 the temperature predictions at 2.5 m, 10 m, 20 m, 30 m, 45 m, 65 m, 85 m, 105 m, 125 m, and 145 m, while at C2, C3 and C4 they are from the first 6, 7 and 9 depths.

small. On the outer shelf and slope, the modeled and predicted means are comparable in the surface layer, but they are different in the subsurface layer. It is obvious that a mean poleward coastal jet and a mean undercurrent on the slope are missing in the model results. The prediction of mean alongshore flow could be significantly improved by including a mean alongshore pressure gradient in the model. This pressure gradient may also make the onshore flow less bottom-trapped. Evidence for a mean alongshore

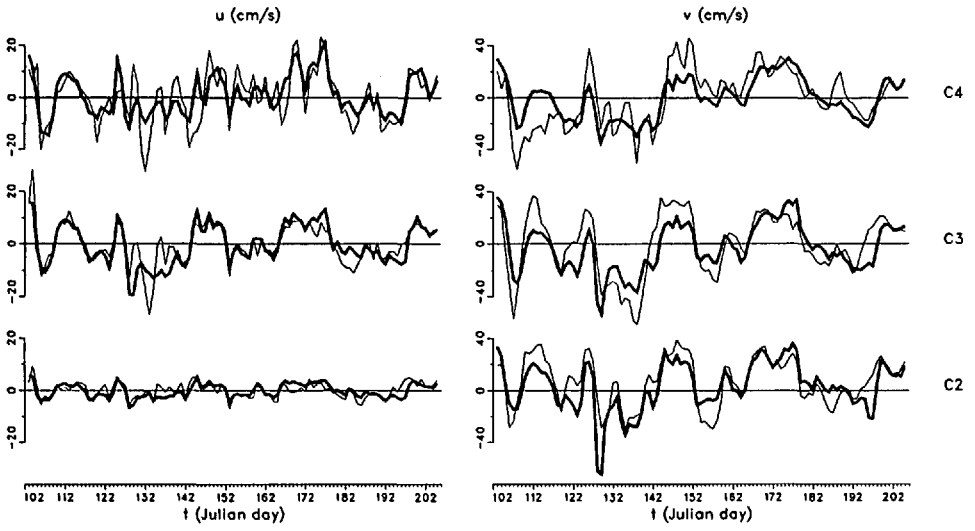

Figure 11. Observed and model-predicted time series of demeaned cross-shelf velocity u and alongshore velocity v at 10 m depth at C2, C3 and C4 moorings. Thin curve is observed and thick curve is predicted.

pressure gradient along the California coast was suggested in Hickey and Pola (1983). On the other hand, the observed standard deviation in alongshore velocities are well predicted, and the correlations between observed and modeled alongshore velocities are generally high. As an example, time series of demeaned alongshore velocities at 10 m depth are shown in Figure 11. The correspondence between modeled and observed velocity variations is generally good, but the variance is sometimes underpredicted, especially during relatively short relaxation events.

6. Discussion

Previous upwelling models have rarely been used to simulate long-term time-variable coastal upwelling using observed meteorological forcing, due to model limitations and lack of data. Hickey and Hamilton (1980) applied a two-dimensional numerical model, in which Munk and Anderson's (1948) model is used for vertical mixing, to a 5-week simulation on the Oregon-Washington continental shelf. They forced the model with the observed wind at a coastal station, but no observed surface heat flux was used in their model. The model worked well in simulating the variations in alongshore velocity although the energy level was underpredicted. By prescribing a buoyancy flux at the surface, they were also able to simulate the displacement of isopycnals. In the present study we simulated a coastal upwelling season on the northern California shelf and slope using a two-dimensional mixing-advection coupled model. Model results compare surprisingly well with CODE 2 moored data, indicating that thermal structures and dynamical processes in the CODE area are mainly

controlled by local forcing, at least during periods of active upwelling. However, it should be pointed out that the model has its limitations because of its two-dimensional nature. For example, the subsurface cross-shelf velocity is not well predicted. It is also evident that the model fails to predict a mean poleward coastal jet. This jet is not important in mass and heat balances during upwelling events, but may advect warm water from the south during wind relaxations when an alongshore temperature gradient is created (Send *et al.*, 1987).

In the heat budget of the upper 35 m layer, the important cooling processes during upwelling periods are vertical mixing and offshore advection of cold water, and the dominant warming process during wind relaxations is solar heating. However, it is noticed that the model-predicted rate of warming is less than the observed. Lentz (1987a) suggested that onshore heat advection is a major cause of the relaxation warming of a shelf-wide water volume with a vertical dimension from the surface to the bottom and an alongshore dimension of 56 km. On the other hand, Send *et al.* (1987) claimed that the surface heating and alongshore heat advection are the dominant warming processes on the inner shelf during relaxations. Moreover, Rudnick and Davis (1988) suggested vertical advection as a major warming process for the surface layer. These different conclusions from the same CODE 2 data may be due to the different water volumes considered and different methods used in estimating the heat balance. Although the cross-shelf advection seems unimportant for the relaxation warming in our model, it is not conclusive since the model is purely two-dimensional. The relative importance of different warming processes can be adequately analyzed only in a three-dimensional model.

One interesting finding from this study is the double-cell circulation associated with the upwelling front. Although the circulation pattern bears some resemblance to that proposed by Mooers *et al.* (1976), the mechanism is not as they suggested. They explained the double-cell as a result of the combination of friction and a strong thermal wind. It was also proposed by Kundu (1984) that the double-cell is generated by internal friction related to high shears of along-front currents at the bottom of the thermocline, and the double-cell (or flow reversal) will disappear if the frictional balance is invalidated, say, by adding an alongshore pressure gradient. In our case, however, the double-cell circulation is clearly generated by the convergence and divergence of the upper layer transport, associated with the anomalous deepening of the surface mixed layer at the front. Thus the double-cell circulation is a transient feature and is not dependent on alongshore currents. Actually, the pattern is not changed in a test run with an alongshore slope included.

The present model is far superior to models based on coastal-trapped wave theory in simulating cross-shelf circulation and thermal structures, which are of primary importance in understanding the exchange processes between coastal water and open ocean. For example, unlike our model, the wind-forced, coastal-trapped wave model of Chapman (1987) has no skill in prediction of cross-shelf velocity and temperature

fluctuations in the CODE area. On the other hand, the long-wave model is adequate in simulating bottom pressure and alongshore current variability, though it underpredicts the variance and fails to predict the vertical shears of alongshore currents on the shelf. Chapman (1987) suggested that the difficulty may be caused by the omission of mixed-layer dynamics. Indeed, the variance and the vertical structure of alongshore currents are better predicted in our model, although the alongshore flow fluctuation is still underpredicted during wind relaxations. This underprediction may be attributed to mesoscale variabilities associated with short-scale wind forcing. A logical next step to coastal upwelling simulation will be to extend the present model to three-dimensions to take full account of mixing, advection and alongshore variability.

Acknowledgments. This work is partially supported by the Institute for Naval Oceanography. We thank Drs. R. C. Beardsley and S. J. Lentz for providing hourly moored data. We also thank Dr. K. Brink for his helpful comments on the manuscript. The model computation is supported by the Cornell National Supercomputer Facilities.

REFERENCES

Adamec, D. and R. W. Garwood. 1985. The simulated response of an upper-ocean density front to local atmospheric forcing. J. Geophys. Res., *90,* 917–928.

Beardsley, R. C. 1986. The surface heat flux over the northern California shelf during spring and summer, 1982. EOS Trans., (abstract) *67,* 1032.

Beardsley, R. C., C. A. Alessi, and R. Limeburner. 1985. CODE-2: Coastal and moored meteorological observations, in CODE-2 Moored Array and Large Scale Data Report, WHOI Tech. Rep. 85–35; R. Limeburner, ed., Woods Hole Oceanogr. Inst., Woods Hole, MA, 23–72.

Chapman, D. C. 1987. Application of wind-forced, long, coastal-trapped wave theory along the California coast. J. Geophys. Res., *92,* 1798–1816.

Chen, D., S. G. Horrigan and D-P. Wang. 1988. The late summer vertical nutrient mixing in Long Island Sound. J. Mar. Res., *46,* 753–770.

Clancy, R. M. and K. D. Pollak. 1983. A real-time synoptic ocean thermal analysis/forecast system. Prog. Oceanog., *12,* 383–424.

de Szoeke, R. A. and J. G. Richman. 1981. The role of wind-generated mixing in coastal upwelling. J. Phys. Oceanogr., *11,* 1534–1547.

—— 1984. On wind-driven mixed layers with strong horizontal gradients—a theory with application to coastal upwelling. J. Phys. Oceanogr., *14,* 364–377.

Fofonoff, N. P. 1962. Physical properties of sea-water, *in* The Sea, *1,* Wiley-Interscience, 3–30.

Hickey, B. M. and P. Hamilton. 1980. A spin-up model as a diagnostic tool for interpretation of current and desnity measurements on the continental shelf of the Pacific Northwest. J. Phys. Oceanogr., *10,* 12–24.

Hickey, B. M. and N. E. Pola. 1983. The seasonal alongshore pressure gradient on the west coast of the United States. J. Geophys. Res., *88,* 7623–7633.

Irish, J. D. 1985. CODE-2: moored temperature and conductivity observations, in CODE-2 Moored Array and Large Scale Data Report, WHOI Tech. Rep. 85-35, R. Limeburner, ed., Woods Hole Oceanogr. Inst., Woods Hole, MA, 133–164.

Kundu, P. K. 1984. Numerical calculations of coastal flow with turbulent dynamics. Deep-Sea Res., *31,* 39–60.

Lentz, S. J., 1987a. A heat budget for the northern California shelf during CODE 2. J. Geophys. Res., *92,* 14,491–14,509.

—— 1987b. A description of the 1981 and 1982 spring transition over the northern California shelf. J. Geophys. Res., *92,* 1545–1567.

Mellor, G. L. and T. Yamada. 1974. A hierarchy of turbulence closure models for planetary boundary layers. J. Atm. Sci., *31,* 1791–1806.

Mooers, C. N. K., C. A. Collins and R. L. Smith. 1976. The dynamic structure of the frontal zone in the coastal upwelling region. J. Phys. Oceanogr., *6,* 3–21.

Munk, W. H. and E. R. Anderson. 1948. Notes on a theory of thermocline. J. Mar. Res., *7,* 276–295.

Niiler, P. P. 1969. On the Ekman divergence in an oceanic jet. J. Geophys. Res., *74,* 7048–7052.

Rosenfeld, L. K. 1988. Diurnal period wind stress and current fluctuations over the continental shelf off northern California. J. Geophys. Res., *93,* 2257–2276.

Rudnick, D. L. and R. E. Davis. 1988. Mass and heat budgets on the northern California continental shelf. J. Geophys. Res., *93,* 14,013–14,024.

Samelson, R. M. and R. A. de Szoeke. 1988. Semigeostrophic wind-driven thermocline upwelling at a coastal boundary. J. Phys. Oceanogr., *18,* 1372–1383.

Send, U., R. C. Beardsley and C. D. Winant. 1987. Relaxation from upwelling in the Coastal Ocean Dynamics Experiment. J. Geophys. Res., *92,* 1683–1689.

Wang, D.-P. 1982. Development of a three-dimensional limited-area (island) shelf circulation model. J. Phys. Oceanogr., *12,* 605–617.

—— 1985. Numerical study of gravity currents in a channel. J. Phys. Oceanogr., *15,* 299–305.

Winant, C. D., U. Send and S. J. Lentz. 1985. CODE-2: moored current observations, in CODE-2 Moored Array and Large Scale Data Report, WHOI Tech. Rep. 85-35, R. Limeburner, ed., Woods Hole Oceanogr. Inst., Woods Hole, MA, 73–108.

Received: *9 October, 1989;* revised: *16 February, 1990.*